

See discussions, stats, and author profiles for this publication at: <https://www.researchgate.net/publication/281494562>

Determination of the Surface Charge Density of Colloidal Gold Nanoparticles Using Second Harmonic Generation

ARTICLE in THE JOURNAL OF PHYSICAL CHEMISTRY C · JUNE 2015

Impact Factor: 4.77 · DOI: 10.1021/acs.jpcc.5b00568

CITATIONS

3

READS

54

3 AUTHORS:



Raju Ram Kumal

Louisiana State University

4 PUBLICATIONS 3 CITATIONS

SEE PROFILE



Tony Karam

Louisiana State University

12 PUBLICATIONS 27 CITATIONS

SEE PROFILE



Louis H. Haber

Louisiana State University

31 PUBLICATIONS 812 CITATIONS

SEE PROFILE

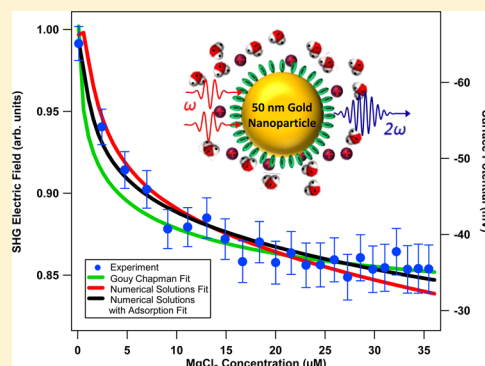
Determination of the Surface Charge Density of Colloidal Gold Nanoparticles Using Second Harmonic Generation

Raju R. Kumal, Tony E. Karam, and Louis H. Haber*

Department of Chemistry, Louisiana State University, Baton Rouge, Louisiana 70803, United States

S Supporting Information

ABSTRACT: Second harmonic generation is used to investigate the surface charge density of 50 nm colloidal gold nanoparticles in water. The gold nanoparticles are thiolated with mercaptosuccinic acid and are dialyzed in ultrapure water to remove excess salts and reactants. The second harmonic generation signal from the nanoparticle sample is measured as a function of added sodium chloride and magnesium chloride salt concentrations using the $\chi^{(3)}$ technique. The experimental results are fit to the Gouy–Chapman model and to numerical solutions to the spherical Poisson–Boltzmann equation that account for the nanoparticle surface curvature, the different salt valences, and ion adsorption to the Stern layer interface. The best fits use the numerical solutions including ion adsorption and determine the initial surface charge density to be $(-2.0 \pm 0.1) \times 10^{-3} \text{ C/m}^2$ at the gold nanoparticle surface, in agreement with electrophoretic mobility measurements. In addition, the sodium ion is observed to adsorb with a higher surface charge density than the magnesium ion. These results demonstrate the important effects of surface curvature and ion adsorption in describing the surface chemistry and surface charge density of colloidal gold nanoparticles in water.



INTRODUCTION

Gold nanoparticles have attracted considerable attention due to their unique physical, chemical, and optical properties,^{1–3} making them well suited for many biological applications such as molecular sensing,^{4,5} labeling,^{6,7} drug delivery,^{8–10} and photothermal cancer therapy.^{11–14} Gold nanoparticles have localized surface plasmon resonances, which are characterized by the coherent oscillations of free electrons under incident light and depend on the nanoparticle size, shape, composition, and surrounding medium.^{1–3} The plasmon resonances can cause significant optical field enhancements leading to processes such as surface enhanced Raman spectroscopy (SERS),^{15,16} surface enhanced fluorescence,^{17–19} and plasmon–exciton polariton resonant coupling.^{20,21} Functionalization of gold nanoparticles with biologically relevant molecules such as proteins, DNA, and pharmaceuticals is readily accessible through thiolation.^{2,22} In order to develop and optimize potential applications of gold nanoparticles, it is important to more fully understand the surface chemistry and surface charge density of colloidal gold nanoparticles in water.

Second harmonic generation (SHG) is a powerful, non-invasive, surface-sensitive technique that is useful for the investigation of colloidal nanoparticles.^{21,23–28} SHG is a nonlinear optical process in which two incident photons of frequency ω add coherently to generate a photon of frequency 2ω .^{29–31} SHG is typically forbidden in bulk media that have inversion symmetry but it can be generated at the surface of nanoparticles where the inversion symmetry is broken. The SHG signal from an interface has contributions from the

second-order and third-order nonlinear susceptibilities, $\chi^{(2)}$ and $\chi^{(3)}$, respectively.^{23,32–34} The $\chi^{(2)}$ term originates from the two-photon spectroscopy of the surface, whereas the $\chi^{(3)}$ term is a consequence of the electric field of the surface inducing a polarization of bulk molecules in the solvent. The surface charge density and the electrostatic surface potential of colloidal nanoparticles can be obtained by fitting experimental SHG measurements as a function of added electrolyte concentrations to theoretical models, such as the Gouy–Chapman model.^{33–36} Several different colloidal nanoparticle samples have been investigated using this SHG $\chi^{(3)}$ method, also called the electric field induced second harmonic (EFISH) technique, including polystyrene nanoparticles,^{32,34,37,38} clay nanodisks,^{23,39} liposomes,⁴⁰ and biologically conjugated nanoparticles.⁴¹ Additional $\chi^{(3)}$ studies have been conducted on planar interfaces including electrolytes near solid/water interfaces,^{33,42,43} DNA at surfaces in solution^{44–46} and hot electron transfer dynamics from colloidal lead selenide nanocrystals to a titanium oxide surface.⁴⁷ For colloidal particles with nanoscale size, consideration of the surface curvature is crucial for an accurate determination of the surface charge density and the electrostatic surface potential, especially in the limit where the Gouy–Chapman model is no longer valid.^{36,48–50}

Existing techniques for obtaining the electrostatic surface potential of colloids based on electrophoretic mobility

Received: January 19, 2015

Revised: May 19, 2015

Published: June 18, 2015

measurements are challenging due to the lack of information regarding the surface structure and its interaction with the solution.^{35,51} For example, problems can arise from accurately accounting for the position of the slipping plane, the double layer distortion, the viscoelectric constant of the solution, and the electroosmosis effect.^{35,51} The relationship between the colloidal surface potential and the corresponding surface charge density depends on several interconnected factors including the nanoparticle size and electrolyte adsorption to the Stern–layer interface.^{35,36,49,50} Previous investigations using electrophoretic mobility measurements on colloidal gold nanoparticles^{49,50} have several inherent experimental limitations and may not correctly account for effects due to nanoparticle aggregation. The direct comparison between results obtained by the SHG $\chi^{(3)}$ method and electrophoretic mobility measurements with careful considerations of nanoparticle size and ion adsorption can provide for the most accurate determination of the surface charge density of colloidal nanoparticles.

In this paper, second harmonic generation measurements are used to determine the surface charge density of 50 nm colloidal gold nanoparticles functionalized with mercaptosuccinic acid (MSA) in water. The SHG signal is measured as a function of added NaCl and MgCl_2 electrolyte concentrations and the results are fit to numerical solutions to the Poisson–Boltzmann equation to account for the nanoparticle surface curvature, the different salts valences, and ion adsorption, with excellent agreement to corresponding electrophoretic mobility measurements. To the best of our knowledge, this is the first time the SHG $\chi^{(3)}$ technique has been successfully integrated with numerical solutions that account for corrections due to the colloidal nanoparticle surface curvature. The findings indicate that a significant Stern layer of counterions is present at the nanoparticle surface and is an important contribution for understanding the surface chemistry of colloidal gold nanoparticles in water.

EXPERIMENTAL SECTION

Synthesis and Characterization of Nanoparticles. The colloidal gold nanoparticle sample is prepared using a technique described previously, which includes seeded growth, thiolation, and dialysis.^{21,52} In the gold nanoparticle seed synthesis, 900 μL of 34 mM sodium citrate is added to 30 mL of 290 μM gold chloride in ultrapure water under boiling conditions and vigorous stirring. The solution changes color to a bright red after 10 min and is then cooled to room temperature. In a separate flask, 250 μL of the seed solution is added to 300 μM of gold chloride in 9.8 mL of ultrapure water, followed by the addition of 100 μL of 0.03 M hydroquinone and 22 μL of 34 mM sodium citrate. The solution is left to stir at room temperature for 60 min to produce the 50 nm colloidal gold nanoparticles.^{21,52} This synthesis procedure is repeated several times until a sufficient sample volume is prepared. The colloidal gold nanoparticles are then dialyzed against a 22 mM solution of MSA in ultrapure water for three consecutive days, followed by dialysis against ultrapure water for 2 additional days, where the outer solution or water is replaced several times a day. The MSA replaces the citrate as the capping agent due to the relatively strong gold–thiol bond. The final dialysis in ultrapure water removes excess salts and reactants from the gold nanoparticle solution.

The gold nanoparticles are characterized using transmission electron microscopy (TEM), dynamic light scattering, ultraviolet–visible extinction spectroscopy, and ζ potential measure-

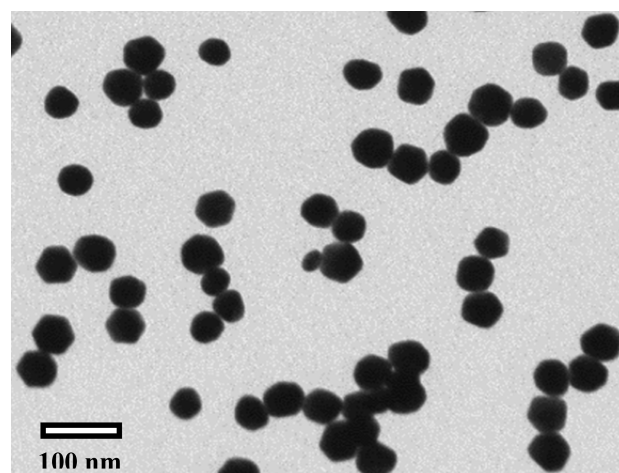


Figure 1. Transmission electron microscopy image of the gold nanoparticle sample. The nanoparticle diameter is determined to be 50 ± 6 nm from a survey of 190 images.

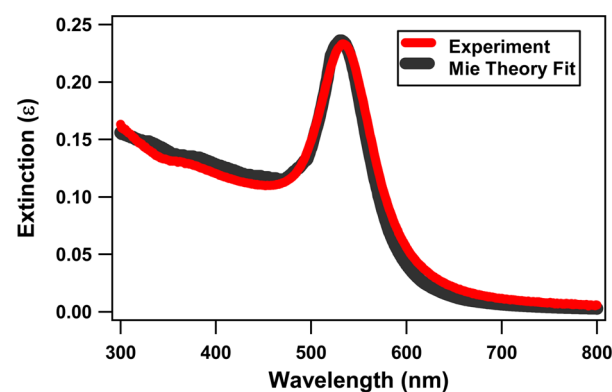


Figure 2. Extinction spectrum of the 50 nm colloidal gold nanoparticle sample in water (red line) compared with the best fit from Mie theory (gray line).

ments. A representative TEM image of the gold nanoparticle sample is shown in Figure 1. From a survey of 190 TEM images, the average nanoparticle size is determined to be 50 ± 6 nm in diameter. Figure 2 displays the experimental extinction spectrum of the diluted colloidal gold nanoparticle sample (red line) compared to the spectrum derived using Mie theory²⁵ for 50 ± 6 nm gold nanoparticles in water (gray line) at a concentration of 2.9×10^9 nanoparticles per mL, showing good agreement. From this result, the concentration of the stock gold nanoparticle sample is determined to be 1.8×10^{10} nanoparticles per mL. The localized surface plasmon peak is observed at 534 nm. Dynamic light scattering measurements of the nanoparticle sample give a hydrodynamic diameter of 50.5 ± 9.6 nm, in agreement with the TEM and extinction spectroscopy results.

The zeta potential ζ of the colloidal gold nanoparticle sample is obtained from electrophoretic mobility measurements using a Malvern Zetasizer (ZEN 3600). The electrophoretic mobility plot showing the average of measurements and the experimental uncertainty is displayed in Figure 3. The relationship between the ζ potential and the electrophoretic motility is given by $U_E = 2e\zeta f(\kappa a)/3\eta$ where, U_E is the electrophoretic mobility, ϵ is the dielectric constant of the bulk solution, η is the coefficient of viscosity of the solvent, $f(\kappa a)$ is Henry's function, κ is the inverse of the Debye length, and a is

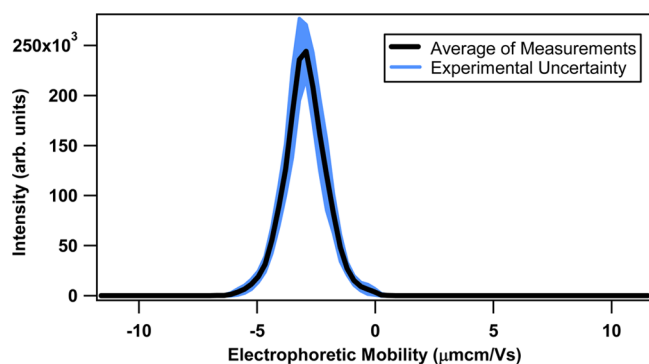


Figure 3. Electrophoretic mobility plot showing the average of measurements (black line) and the experimental uncertainty (blue error bars).

the nanoparticle radius. For $\kappa a \ll 1$, Huckel's approximation gives $f(\kappa a) = 1$.^{50,53} For our experimental conditions, before adding any salts, $\kappa a \ll 1$, so Huckel's approximation is used. For the colloidal gold nanoparticle sample in water, with a diameter of 50 ± 6 nm, the average electrophoretic mobility is measured to be $-2.96 \pm 0.89 \mu\text{m cm}/(\text{V s})$, giving a ζ potential of -57 ± 17 mV.

Experimental Setup. The experimental setup for the second harmonic generation studies has been described previously.^{21,25} Briefly, the setup consists of an ultrafast laser system, an optical setup, and a high-sensitivity charge-coupled device spectroscopy detector connected to a monochromator–spectrograph. A titanium:sapphire oscillator laser with 2.6 W average power and 70 fs pulses centered at 800 nm with a repetition rate of 80 MHz is attenuated to 1.2 W and is focused to the gold nanoparticle sample at an initial concentration of 4.4×10^9 nanoparticles per mL in a 1 cm quartz cuvette. Optical filters are used to remove any residual SHG signal from the laser beam before hitting the sample and to remove the fundamental 800 nm light after the sample. The SHG signal is acquired in the forward direction from the nanoparticle sample. An integrated computer program controls a beam block, a magnetic stir bar, and a buret to add the salt solutions to the sample under stirring in synchronization with automated data acquisition for background-subtracted concentration-dependent SHG measurements. Multiple spectra are acquired with 1 s acquisitions for the laser blocked and unblocked for 1 min for each salt concentration for statistical analysis.

RESULTS AND DISCUSSION

The background-subtracted concentration-dependent SHG spectra are analyzed in order to obtain the SHG electric field as a function of the added salt concentration for both NaCl and MgCl_2 . Representative SHG spectra of colloidal gold nanoparticles with added NaCl and MgCl_2 are shown in Figure 4, parts a and b, respectively. The large SHG peak is centered at 400 nm and has a full width half-maximum of 4.5 nm. The rise in intensity at longer wavelengths is attributed to two-photon fluorescence from the colloidal gold nanoparticles. The SHG signal is observed to decrease with added salt concentrations due, in part, to the changing electrostatic potential at the gold nanoparticle surface and the corresponding $\chi^{(3)}$ effect. The SHG electric field E_{SHG} is proportional to the square root of the SHG signal, where

$$E_{\text{SHG}} = A + B\Phi_0 \quad (1)$$

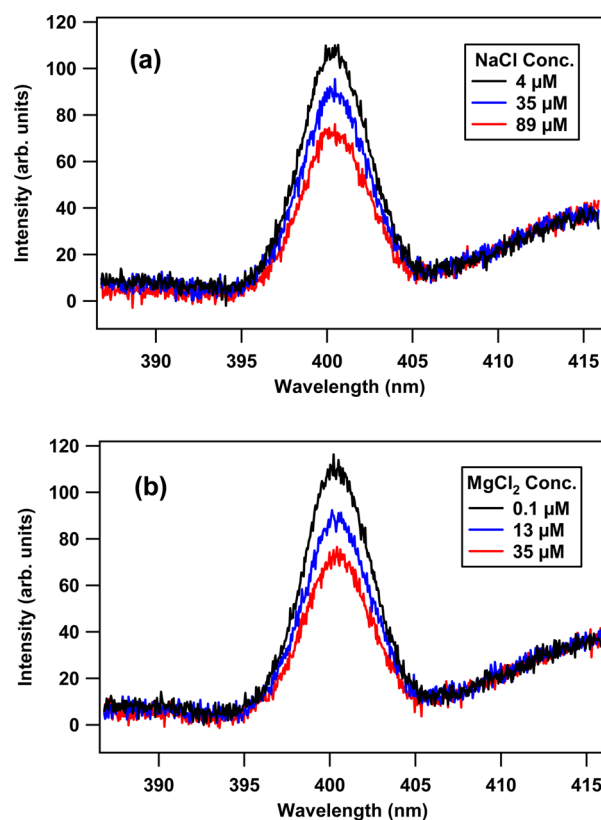


Figure 4. SHG spectra of the colloidal gold nanoparticle sample at different (a) NaCl and (b) MgCl_2 concentrations using 800 nm incident light.

Here, A and B are constants that include the second-order and third-order nonlinear susceptibilities, $\chi^{(2)}$ and $\chi^{(3)}$, respectively, as well as the incident electric field E_ω from the laser at frequency ω . As the electrolyte concentration is increased, the ions distribute around the charged surface and screen the electrostatic potential Φ_0 at the nanoparticle surface to decrease its magnitude, which leads to a decrease in the measured SHG signal.

In order to distinguish between the SHG decrease from the $\chi^{(3)}$ effect with the SHG decrease due to nanoparticle dilution, the results are compared to a control where ultrapure water is added to the nanoparticle sample instead of the salt solutions. The SHG signal from the sample at different concentrations is obtained by integrating the background-subtracted spectrum over the wavelength range from 395 and 405 nm and subtracting a two-photon fluorescence linear offset connecting the spectra from 394 to 395 nm and from 405 to 406 nm using a linear least-squares fit. The background-corrected SHG signal of the gold nanoparticle sample as a function of the added volume of water, 0.25 mM NaCl, and 0.10 mM of MgCl_2 is shown in Figure 5. Error bars represent the standard deviation of the SHG signal. The SHG signal is observed to decrease when adding water alone due to nanoparticle dilution. The SHG signal is observed to decrease much more, especially at first, when adding the NaCl and MgCl_2 solutions due to a combination of nanoparticle dilution and the $\chi^{(3)}$ effect. When adding water to the gold nanoparticle sample, the SHG signal is observed to vary linearly with the nanoparticle concentration, as expected for this concentration range. Figure 6 shows these results, with the best fit (red line) given by a slope of $(1.72 \pm 0.02) \times 10^{-10}$ mL/nanoparticle and a y -intercept of $0.246 \pm$

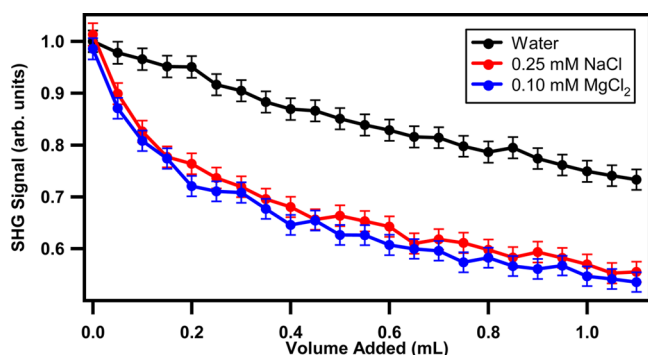


Figure 5. SHG signal of the gold nanoparticle sample as a function of the added volume of ultrapure water (black line), 0.25 mM NaCl (red line), and 0.10 mM MgCl₂ (blue line).

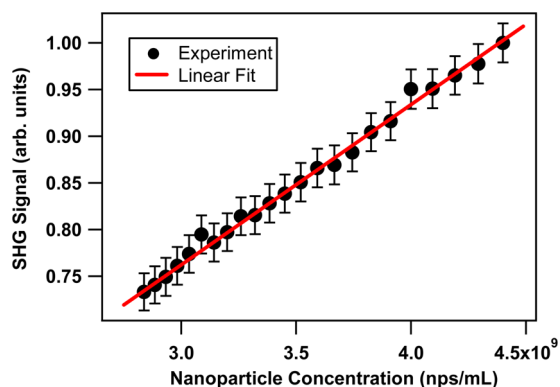


Figure 6. SHG signal intensity as a function of the concentration of the gold nanoparticle sample in water.

0.008 in arbitrary units where the SHG signal is normalized for the initial sample concentration. The nonzero y -intercept is due to SHG signal from water alone in the quartz cuvette. The corrected SHG signal due to the $\chi^{(3)}$ effect is determined by dividing the measured SHG signal as a function of the added salt solution volume by the linear decrease obtained from the added water measurements. The square root of the corrected SHG signal is denoted as the SHG electric field E_{SHG} , which is used to compare to theoretical model best fits. Complementary SHG and extinction spectroscopy measurements of the gold nanoparticle sample as a function of higher salt concentrations are shown in the Supporting Information and demonstrate that nanoparticle aggregation and plasmonic spectral shifts do not occur in the concentration range studied in Figures 4, 5, and 7.⁵⁴ The SHG signal is observed to increase significantly for nanoparticle aggregation, in contrast to the decrease in SHG signal from the $\chi^{(3)}$ effect, measured here.

The surface charge density and the electrostatic surface potential of the colloidal gold nanoparticles capped with MSA is obtained by fitting the concentration-dependent experimental measurements of E_{SHG} to three different models. The first model is the Gouy–Chapman model,^{34,35} which is expected to be extremely inaccurate for the nanoparticle sizes studied here. The second and third models use numerical solutions to the spherical Poisson–Boltzmann equation,^{34–36,48} and either neglect ion adsorption or include ion adsorption, respectively. The Poisson–Boltzmann equation is given by

$$\nabla^2 \Phi = -\frac{eN_A}{\epsilon} \sum_i C_i z_i e^{-z_i e \Phi / kT} \quad (2)$$

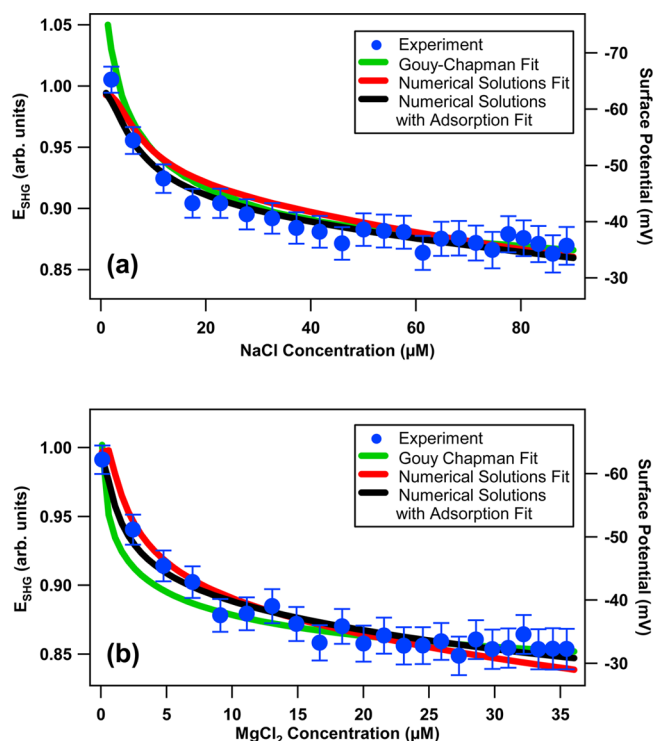


Figure 7. Experimental measurements of the SHG electric field (blue circles) as a function of added (a) NaCl and (b) MgCl₂ salt concentrations for the colloidal gold nanoparticle sample with corresponding fits using the Gouy–Chapman model (green curves) and numerical solutions to the Poisson–Boltzmann equation without ion adsorption (red curves) and with ion adsorption (black curves).

where Φ is the electrostatic potential as a function of the distance from the surface, e is the elementary charge, N_A is the Avogadro constant, C_i is the bulk electrolyte concentration of the i th ion, z_i is the charge of the i th ion, k is the Boltzmann constant, and T is the temperature. The Gouy–Chapman model is the analytical solution to the Poisson–Boltzmann equation for describing the distributions of ions near a planar, charged surface in a symmetric electrolyte solution. The surface potential, according to the Gouy–Chapman model, is given by

$$\Phi_0 = \frac{2kT}{ze} \sinh^{-1} \left(\frac{\sigma}{\sqrt{8ekTC}} \right) \quad (3)$$

where σ is the surface charge density in SI units and C is the salt concentration. NaCl is a symmetric electrolyte with $z = 1$. MgCl₂ is an asymmetric electrolyte so the GC model is an inaccurate description of the electrostatic surface potential under varying MgCl₂ concentration, especially under certain conditions. For a negatively charged planar surface at relatively low concentrations, the Mg²⁺ ion dominates the interaction and the GC equation with $z = 2$ is sufficiently accurate for modeling the surface potential in the MgCl₂ electrolyte solution. However, for nanoparticles smaller than about 100 nm, the significant surface curvature requires a numerical solution to the Poisson–Boltzmann equation in spherical coordinates in order to accurately determine the relationship between the surface charge density and the electrostatic surface potential in an electrolyte.^{49,50} In addition, ion adsorption to the colloidal nanoparticle surface can be included by expressing the surface charge density as the sum of the initial surface charge density σ_0 and the charge density created by adsorbed ions, given by^{33,55}

Table 1. Summary of the Fitting Results of A , B , and σ for the Three Models^a

models	fit parameters			initial surface potential (mV)	
	A	B (V ⁻¹)	σ (C/m ²)	NaCl	MgCl ₂
Gouy–Chapman	0.810 ± 0.004	-2.11 ± 0.08	$(-6.08 \pm 0.57) \times 10^{-4}$	-93 ± 6	-86 ± 6
numerical solutions	0.659 ± 0.008	-7.49 ± 0.25	$(-1.36 \pm 0.12) \times 10^{-3}$	-46 ± 2	-42 ± 2
numerical solutions with adsorption	0.706 ± 0.009	-4.59 ± 0.16	$(-1.95 \pm 0.12) \times 10^{-3}$	-65 ± 2	-62 ± 2

^aThe resulting initial surface potentials before adding salts are also tabulated.

$$\sigma = \sigma_0 + \sigma_m \left(\frac{K_m C}{1 + K_m C} \right) \quad (4)$$

where σ_m is the maximum surface charge density due to adsorbed ions m at saturation and K_m is the equilibrium constant of ion adsorption. In this case, the surface potential corresponds to the outer edge of the Stern layer, including the adsorbed ions.

The three different models are applied to fit the experimental E_{SHG} measurements of the gold nanoparticle sample under varying NaCl and MgCl₂ concentrations. Since the data are taken under the same laser and nanoparticle sample conditions, the values for A , B , and σ from eq 1 are expected to remain constant for both the NaCl and MgCl₂ concentration-dependent measurements for each separate fit. The experimental results of the SHG electric field measurements with the corresponding fits as a function of NaCl and MgCl₂ concentrations are shown in Figure 7. The first fit uses eq 3 from the Gouy–Chapman model for $z = 1$ for NaCl and $z = 2$ for MgCl₂ resulting in the green curves for Figure 7, parts a and b, with A , B , and σ given by 0.810 ± 0.004 , -2.11 ± 0.08 V⁻¹, and $(-6.08 \pm 0.57) \times 10^{-4}$ C/m², respectively. However, it is important to point out again that the Gouy–Chapman model is not expected to be valid for the nanoparticle size and salt concentrations in these studies. The second fit incorporates numerical calculations for the Poisson–Boltzmann equation and neglects ion adsorption. The numerical calculations include effects from the nanoparticle surface curvature and the symmetric and asymmetric NaCl and MgCl₂ electrolytes. More details about the procedure used for the numerical solutions to the spherical Poisson–Boltzmann equation and the corresponding fits are described in the Supporting Information. The second fit using the numerical solutions to the Poisson–Boltzmann equation without including ion adsorption is shown by the red curves in Figure 7, parts a and b, with A , B , and σ given by 0.659 ± 0.008 , -7.49 ± 0.25 V⁻¹, and $(-1.36 \pm 0.12) \times 10^{-3}$ C/m², respectively. The third fit using the numerical solutions to the Poisson–Boltzmann equation including ion adsorption is shown by the black curves in Figure 7, parts a and b, with A , B , and σ_0 given by 0.706 ± 0.009 , -4.59 ± 0.16 V⁻¹, and $(-1.95 \pm 0.12) \times 10^{-3}$ C/m², respectively, with the ion adsorption surface densities and equilibrium constants given by $2.6 \pm 0.5 \times 10^{-4}$ C/m² and 0.18 μM⁻¹, respectively, for the sodium ion, and $1.3 \pm 0.5 \times 10^{-4}$ C/m² and 11 μM⁻¹, respectively, for the magnesium ion. The fitting results are summarized in Table 1. The third fit, using the numerical solutions including ion adsorption, provides the best accuracy to the experimental results, giving an overall R^2 value of 0.95, compared to R^2 values of 0.92 and 0.90 for the first and second fits, respectively. Accordingly, the adjusted \bar{R}^2 values are 0.92, 0.90, and 0.94 for the first, second, and third fits, respectively, showing that the third fit is still the most accurate model when considering the different number of fitting parameters.

The corresponding surface potentials from the best fit using numerical solutions to the spherical Poisson–Boltzmann equation including ion adsorption are labeled on the right-side y-axes of Figure 7, parts a and b. The surface potentials before the addition of salts from this best fit are determined to be -65 ± 2 and -62 ± 2 mV for the NaCl and MgCl₂ data sets, respectively. In comparison, the corresponding surface potentials from the other fits before the addition of salts are -46 ± 2 and -42 ± 2 mV for the NaCl and MgCl₂ data sets using the numerical solutions fit without including adsorption, respectively, and -93 ± 6 and -86 ± 6 mV for the NaCl and MgCl₂ data sets using the Gouy–Chapman fit, respectively. In addition, the low electrolyte concentrations studied here lead to large Debye lengths, so the ζ potential is not expected to deviate by more than about 5% from the surface potential before adding salt, since electroviscosity effects can be neglected and the distance from the surface to the slipping plane can be estimated to be about 1 nm.^{56,57} The ζ potential of the gold nanoparticles obtained from the electrophoretic mobility measurements shown in Figure 3 agrees best with the initial surface potentials determined from the numerical solutions including adsorption, further confirming the accuracy of this model. Taking these considerations into account, the σ value of $(-1.95 \pm 0.12) \times 10^{-3}$ C/m², obtained from numerical solutions to the Poisson–Boltzmann equation including ion adsorption, is expected to represent the most accurate determination of the surface charge density of this gold nanoparticle sample in water. This corresponds to a total charge of $(-1.53 \pm 0.09) \times 10^{-17}$ C or -95.6 ± 5.9 charges per nanoparticle.

The ion adsorption surface densities and equilibrium constants obtained from the best fit provide interesting insight into the nature of the colloidal gold nanoparticle surface. The higher ion adsorption surface charge density of the sodium ion compared to the magnesium ion can be explained predominantly by the different values of the free energy of solvation, where the Na⁺ ion has a solvation free energy of -375 kJ/mol in water and the Mg has a solvation free energy of -1838 kJ/mol.⁵⁸ The larger ion adsorption equilibrium constant of magnesium compared to sodium can be explained by the different valences of the ions. Additional factors such as ion polarizabilities, adsorbate–adsorbate repulsions, and image–charge attraction probably also influence these results.

These experimental results provide an important description of the colloidal gold nanoparticle interface. The results indicate that ion adsorption is important at the colloidal gold nanoparticle interface in water. Additionally, previous studies estimate the average area of MSA to be 15 Å² in a self-assembled monolayer (SAM).^{49,59} The nanoparticles are expected to be covered by a full monolayer of MSA since the nanoparticles are prepared by dialysis in an MSA solution in significant excess of the concentration needed to saturate the gold surface, although additional studies should be done to confirm this. The first and second acid dissociation constants

for MSA in water are given by $\text{p}K_{a1} = 4.19$ and $\text{p}K_{a2} = 5.64$.⁴⁹ The pH of the gold nanoparticle sample is measured to be 6.0 ± 0.2 . Therefore, assuming full coverage, each MSA molecule would have an average charge of $-1.7 \pm 0.1 e$, assuming the acid dissociation constants are the same when the molecule is attached to the gold nanoparticle surface. Using the expected MSA molecular density from SAM studies, this would correspond to a surface charge density of -1.7 C/m^2 . The significant discrepancy between this estimated surface charge density and the measured value using the $\chi^{(3)}$ method can be explained by several factors. The $\text{p}K_a$ of MSA is likely to be very different at the nanoparticle surface than in bulk water, leading to a lower surface charge density. The MSA may not form a full monolayer at the nanoparticle surface. Gold atoms near the surface may be positively charged, offsetting the total charge of the nanoparticle. Additionally, adsorbed counterions may be present on the gold nanoparticle surface even before adding any salt concentration. Theoretical modeling of metal surfaces in electrolytes indicates that image-charge attraction can significantly increase Stern layer concentrations of counterions.⁶⁰ This contrasts with surfaces of materials with lower dielectric constants than water, which are characterized by image-charge repulsion in aqueous electrolyte solutions.⁶¹ The organic monolayer will also alter any image-charge effects. More work is needed to fully characterize the surface chemistry of the colloidal gold nanoparticles for improving the functionality for applications such as molecular sensing, nanomedicine, and catalysis.

CONCLUSION

Second harmonic generation is used to obtain the surface charge density of 50 nm gold nanoparticles functionalized with MSA in aqueous colloidal suspension. The experimental results of the SHG electric field as a function of added NaCl and MgCl_2 concentrations are most accurately described using the $\chi^{(3)}$ technique with a model based on numerical solutions to the spherical Poisson–Boltzmann equation which account for the nanoparticle surface curvature, salt valences, and ion adsorption. The best fit of the SHG data determines that the surface charge density of the gold nanoparticles is $(-2.0 \pm 0.1) \times 10^{-3} \text{ C/m}^2$, which corresponds to a total charge of -96 ± 6 per nanoparticle. These results agree with corresponding electrophoretic mobility measurements. In addition, the sodium ion is observed to adsorb with a higher saturated surface charge density compared to the magnesium ion, even though the magnesium ion is observed to have a larger equilibrium constant of adsorption, which is likely the consequence of the different cation valences and solvation free energies. These measurements help to provide an important characterization of the colloidal gold nanoparticle interface for improving potential applications in molecular sensing, nanomedicine, and catalysis.

ASSOCIATED CONTENT

Supporting Information

More details on the fitting models and complementary characterization measurements. The Supporting Information is available free of charge on the ACS Publications website at DOI: 10.1021/acs.jpcc.5b00568.

AUTHOR INFORMATION

Corresponding Author

*(L.H.H.) E-mail: lhaber@lsu.edu. Telephone: 225-578-7965.

Notes

The authors declare no competing financial interest.

ACKNOWLEDGMENTS

Generous financial support for this work was provided by Louisiana State University. The authors acknowledge Professor Kenneth Eissenthal, Dr. Zhenyu Zhang, Emily Harwell, and Sheldon Kwok for many valuable discussions. We are also grateful to Dr. Raphael Cueto for his help with dynamic light scattering and ζ potential measurements and to Dr. Xiaochu Wu for his help with transmission electron microscopy.

REFERENCES

- (1) Eustis, S.; El-Sayed, M. A. Why Gold Nanoparticles are More Precious Than Pretty Gold: Noble Metal Surface Plasmon Resonance and its Enhancement of the Radiative and Nonradiative Properties of Nanocrystals of Different Shapes. *Chem. Soc. Rev.* **2006**, *35*, 209–217.
- (2) Daniel, M.-C.; Astruc, D. Gold Nanoparticles: Assembly, Supramolecular Chemistry, Quantum-Size-Related Properties, and Applications Toward Biology, Catalysis, and Nanotechnology. *Chem. Rev.* **2004**, *104*, 293–346.
- (3) Link, S.; El-Sayed, M. A. Shape and Size Dependence of Radiative, Non-radiative and Photothermal Properties of Gold Nanocrystals. *Int. Rev. Phys. Chem.* **2000**, *19*, 409–453.
- (4) Mayer, K. M.; Hafner, J. H. Localized Surface Plasmon Resonance Sensors. *Chem. Rev.* **2011**, *111*, 3828–3857.
- (5) Saha, K.; Agasti, S. S.; Kim, C.; Li, X.; Rotello, V. M. Gold Nanoparticles in Chemical and Biological Sensing. *Chem. Rev.* **2012**, *112*, 2739–2779.
- (6) Cao, Y. C.; Jin, R.; Mirkin, C. A. Nanoparticles With Raman Spectroscopic Fingerprints for DNA and RNA Detection. *Science* **2002**, *297*, 1536–1540.
- (7) Eck, W.; Craig, G.; Sigdel, A.; Ritter, G.; Old, L. J.; Tang, L.; Brennan, M. F.; Allen, P. J.; Mason, M. D. PEGylated Gold Nanoparticles Conjugated to Monoclonal F19 Antibodies as Targeted Labeling Agents for Human Pancreatic Carcinoma Tissue. *ACS Nano* **2008**, *2*, 2263–2272.
- (8) Casal-Dujat, L.; Rodrigues, M.; Yagüe, A.; Calpena, A. C.; Amabilino, D. B.; González-Linares, J.; Borrás, M.; Pérez-García, L. Gemini Imidazolium Amphiphiles for the Synthesis, Stabilization, and Drug Delivery From Gold Nanoparticles. *Langmuir* **2012**, *28*, 2368–2381.
- (9) Giljohann, D. A.; Seferos, D. S.; Daniel, W. L.; Massich, M. D.; Patel, P. C.; Mirkin, C. A. Gold Nanoparticles for Biology and Medicine. *Angew. Chem., Int. Ed.* **2010**, *49*, 3280–3294.
- (10) Von Maltzahn, G.; Park, J.-H.; Lin, K. Y.; Singh, N.; Schwöppe, C.; Mesters, R.; Berdel, W. E.; Ruoslahti, E.; Sailor, M. J.; Bhatia, S. N. Nanoparticles that Communicate in Vivo to Amplify Tumour Targeting. *Nat. Mater.* **2011**, *10*, 545–552.
- (11) Gao, J.; Huang, X.; Liu, H.; Zan, F.; Ren, J. Colloidal Stability of Gold Nanoparticles Modified With Thiol Compounds: Bioconjugation and Application in Cancer Cell Imaging. *Langmuir* **2012**, *28*, 4464–4471.
- (12) Chen, J.; Wang, D.; Xi, J.; Au, L.; Siekkinen, A.; Warsen, A.; Li, Z.-Y.; Zhang, H.; Xia, Y.; Li, X. Immuno Gold Nanocages With Tailored Optical Properties for Targeted Photothermal Destruction of Cancer Cells. *Nano Lett.* **2007**, *7*, 1318–1322.
- (13) El-Sayed, I. H.; Huang, X.; El-Sayed, M. A. Surface Plasmon Resonance Scattering and Absorption of anti-EGFR Antibody Conjugated Gold Nanoparticles in Cancer Diagnostics: Applications in Oral Cancer. *Nano Lett.* **2005**, *5*, 829–834.
- (14) Clarke, M. L.; Chou, S. G.; Hwang, J. Monitoring Photo-thermally Excited Nanoparticles via Multimodal Microscopy. *J. Phys. Chem. Lett.* **2010**, *1*, 1743–1748.
- (15) Qian, X.; Peng, X.-H.; Ansari, D. O.; Yin-Goen, Q.; Chen, G. Z.; Shin, D. M.; Yang, L.; Young, A. N.; Wang, M. D.; Nie, S. In Vivo Tumor Targeting and Spectroscopic Detection With Surface-

Enhanced Raman Nanoparticle Tags. *Nat. Biotechnol.* **2007**, *26*, 83–90.

(16) Wustholz, K. L.; Henry, A.-I.; McMahon, J. M.; Freeman, R. G.; Valley, N.; Piotti, M. E.; Natan, M. J.; Schatz, G. C.; Duyn, R. P. V. Structure–Activity Relationships in Gold Nanoparticle Dimers and Trimers for Surface-Enhanced Raman Spectroscopy. *J. Am. Chem. Soc.* **2010**, *132*, 10903–10910.

(17) Fu, Y.; Zhang, J.; Lakowicz, J. R. Plasmon-Enhanced Fluorescence From Single Fluorophores End-Linked to Gold Nanorods. *J. Am. Chem. Soc.* **2010**, *132*, 5540–5541.

(18) Bardhan, R.; Grady, N. K.; Cole, J. R.; Joshi, A.; Halas, N. J. Fluorescence Enhancement by Au Nanostructures: Nanoshells and Nanorods. *ACS Nano* **2009**, *3*, 744–752.

(19) Tam, F.; Goodrich, G. P.; Johnson, B. R.; Halas, N. J. Plasmonic Enhancement of Molecular Fluorescence. *Nano Lett.* **2007**, *7*, 496–501.

(20) Cade, N.; Ritman-Meer, T.; Richards, D. Strong Coupling of Localized Plasmons and Molecular Excitons in Nanostructured Silver Films. *Phys. Rev. B* **2009**, *79*, 241404.

(21) Karam, T. E.; Haber, L. H. Molecular Adsorption and Resonance Coupling at the Colloidal Gold Nanoparticle Interface. *J. Phys. Chem. C* **2013**, *118*, 642–649.

(22) Sperling, R. A.; Rivera Gil, P.; Zhang, F.; Zanella, M.; Parak, W. J. Biological Applications of Gold Nanoparticles. *Chem. Soc. Rev.* **2008**, *37*, 1896–1908.

(23) Eienthal, K. B. Second Harmonic Spectroscopy of Aqueous Nano- and Microparticle Interfaces. *Chem. Rev.* **2006**, *106*, 1462–1477.

(24) Haber, L. H.; Eienthal, K. B. Molecular Excited-State Relaxation Dynamics at the Colloidal Microparticle Interface Monitored with Pump-Probe Second Harmonic Generation. *J. Phys. Chem. B* **2013**, *117*, 4249–4253.

(25) Haber, L. H.; Kwok, S. J. J.; Semeraro, M.; Eienthal, K. B. Probing the Colloidal Gold Nanoparticle/Aqueous Interface With Second Harmonic Generation. *Chem. Phys. Lett.* **2011**, *507*, 11–14.

(26) Jen, S.-H.; Dai, H.-L.; Gonella, G. The Effect of Particle Size in Second Harmonic Generation From the Surface of Spherical Colloidal Particles. II: The Nonlinear Rayleigh–Gans–Debye Model. *J. Phys. Chem. C* **2010**, *114*, 4302–4308.

(27) Gonella, G.; Gan, W.; Xu, B.; Dai, H.-L. The Effect of Composition, Morphology, and Susceptibility on Nonlinear Light Scattering From Metallic and Dielectric Nanoparticles. *J. Phys. Chem. Lett.* **2012**, *3*, 2877–2881.

(28) Gonella, G.; Dai, H.-L. Second Harmonic Light Scattering from the Surface of Colloidal Objects: Theory and Applications. *Langmuir* **2013**, *30*, 2588–2599.

(29) Boyd, R. W. *Nonlinear Optics*, 3rd ed.; Academic Press: New York, 2003.

(30) Eienthal, K. B. Liquid Interfaces Probed by Second-Harmonic and Sum-Frequency Spectroscopy. *Chem. Rev.* **1996**, *96*, 1343–1360.

(31) Shen, Y. R. *The Principles of Nonlinear Optics*; Wiley: Hoboken, NJ, 2003.

(32) Schurer, B.; Wunderlich, S.; Sauerbeck, C.; Peschel, U.; Peukert, W. Probing Colloidal Interfaces by Angle-Resolved Second Harmonic Light Scattering. *Phys. Rev. B* **2010**, *82*, 2414041–2414044.

(33) Malin, J. N.; Hayes, P. L.; Geiger, F. M. Interactions of Ca, Zn, and Cd Ions at Buried Solid/Water Interfaces Studied by Second Harmonic Generation. *J. Phys. Chem. C* **2009**, *113*, 2041–2052.

(34) Yan, E. C. Y.; Liu, Y.; Eienthal, K. B. New Method for Determination of Surface Potential of Microscopic Particles by Second Harmonic Generation. *J. Phys. Chem. B* **1998**, *102*, 6331–6336.

(35) Hiemenz, P. C.; Rajagopalan, R. *Principles of Colloid and Surface Chemistry, Revised and Expanded*, 3rd ed.; CRC Press: New York, 1997.

(36) Ohshima, H.; Healy, T. W.; White, L. R. Accurate Analytic Expressions for the Surface Charge Density/Surface Potential Relationship and Double-Layer Potential Distribution for a Spherical Colloidal Particle. *J. Colloid Interface Sci.* **1982**, *90*, 17–26.

(37) Subir, M.; Liu, J.; Eienthal, K. B. Protonation at the Aqueous Interface of Polymer Nanoparticles With Second Harmonic Generation. *J. Phys. Chem. C* **2009**, *113*, 20772–20772.

(38) Wang, H.-f.; Borguet, E.; Yan, E.; Zhang, D.; Gutow, J.; Eienthal, K. Molecules at Liquid and Solid Surfaces. *Langmuir* **1998**, *14*, 1472–1477.

(39) Yan, E. C.; Eienthal, K. B. Probing the Interface of Microscopic Clay Particles in Aqueous Solution by Second Harmonic Generation. *J. Phys. Chem. B* **1999**, *103*, 6056–6060.

(40) Liu, Y.; Yan, C. Y.; Zhao, X. L.; Eienthal, K. B. Surface Potential of Charged Liposomes Determined by Second Harmonic Generation. *Langmuir* **2001**, *17*, 2063–2066.

(41) Doughty, B.; Rao, Y.; Kazer, S. W.; Kwok, S. J.; Turro, N. J.; Eienthal, K. B. Binding of the Anti-Cancer Drug Daunomycin to DNA Probed by Second Harmonic Generation. *J. Phys. Chem. B* **2013**, *117*, 15285–15289.

(42) Chen, E. H.; Saslow, S. A.; Nguyen, S. T.; Geiger, F. M. Zinc Ion–Hydroxyl Interactions at Undecanol-Functionalized Fused Silica/Water Interfaces Using the Eienthal $\chi(3)$ Technique. *J. Phys. Chem. C* **2012**, *116*, 7016–7020.

(43) Malin, J. N.; Holland, J. G.; Saslow, S. A.; Geiger, F. M. U(VI) Adsorption and Speciation at the Acidic Silica/Water Interface Studied by Resonant and Nonresonant Second Harmonic Generation. *J. Phys. Chem. C* **2011**, *115*, 13353–13360.

(44) Boman, F. C.; Gibbs-Davis, J. M.; Heckman, L. M.; Stepp, B. R.; Nguyen, S. T.; Geiger, F. M. DNA at Aqueous/Solid Interfaces: Chirality-Based Detection via Second Harmonic Generation Activity. *J. Am. Chem. Soc.* **2008**, *131*, 844–848.

(45) Holland, J. G.; Jordan, D. S.; Geiger, F. M. Divalent Metal Cation Speciation and Binding to Surface-Bound Oligonucleotide Single Strands Studied by Second Harmonic Generation. *J. Phys. Chem. B* **2011**, *115*, 8338–8345.

(46) Walter, S. R.; Geiger, F. M. DNA on Stage: Showcasing Oligonucleotides at Surfaces and Interfaces With Second Harmonic and Vibrational Sum Frequency Generation. *J. Phys. Chem. Lett.* **2009**, *1*, 9–15.

(47) Tisdale, W. A.; Williams, K. J.; Timp, B. A.; Norris, D. J.; Aydil, E. S.; Zhu, X.-Y. Hot-Electron Transfer From Semiconductor Nanocrystals. *Science* **2010**, *328*, 1543–1547.

(48) Tuinier, R. Approximate Solutions to the Poisson–Boltzmann Equation in Spherical and Cylindrical Geometry. *J. Colloid Interface Sci.* **2003**, *258*, 45–49.

(49) Kimura, K.; Takashima, S.; Ohshima, H. Molecular Approach to the Surface Potential Estimate of Thiolate-Modified Gold Nanoparticles. *J. Phys. Chem. B* **2002**, *106*, 7260–7266.

(50) Makino, K.; Ohshima, H. Electrophoretic Mobility of a Colloidal Particle with Constant Surface Charge Density. *Langmuir* **2010**, *26*, 18016–18019.

(51) Dukhin, S.; Zimmermann, R.; Werner, C. A Concept for the Generalization of the Standard Electrokinetic Model. *Colloids Surf., A* **2001**, *195*, 103–112.

(52) Perrault, S. D.; Chan, W. C. W. Synthesis and Surface Modification of Highly Monodispersed, Spherical Gold Nanoparticles of 50–200 nm. *J. Am. Chem. Soc.* **2009**, *131*, 17042–17043.

(53) Evans, D. F.; Wennerström, H. *The Colloidal Domain: Where Physics, Chemistry, Biology, and Technology Meet*; Wiley-VCH: New York, 1999.

(54) Vance, F. W.; Lemon, B. I.; Hupp, J. T. Enormous Hyper-Rayleigh Scattering From Nanocrystalline Gold Particle Suspensions. *J. Phys. Chem. B* **1998**, *102*, 10091–10093.

(55) Salafsky, J.; Eienthal, K. Protein Adsorption at Interfaces Detected by Second Harmonic Generation. *J. Phys. Chem. B* **2000**, *104*, 7752–7755.

(56) Lyklema, J.; Overbeek, J. T. G. On the Interpretation of Electrokinetic Potentials. *J. Colloid Sci.* **1961**, *16*, 501–512.

(57) Lyklema, J. Molecular Interpretation of Electrokinetic Potentials. *Curr. Opin. Colloid Interface Sci.* **2010**, *15*, 125–130.

(58) Marcus, Y. *Ion Properties*; Marcel Dekker Inc.: New York, 1997.

(59) Chen, S.; Kimura, K. Synthesis and Characterization of Carboxylate-Modified Gold Nanoparticle Powders Dispersible in Water. *Langmuir* **1999**, *15*, 1075–1082.

(60) Brüesch, P.; Christen, T. The Electric Double Layer at a Metal Electrode in Pure Water. *J. Appl. Phys.* **2004**, *95*, 2846–2856.

(61) Hatlo, M. M.; Lue, L. The Role of Image Charges in the Interactions Between Colloidal Particles. *Soft Matter* **2008**, *4*, 1582–1596.